

THERMAL INSTABILITY IN SHEARING AND PERIODIC TURBULENCE

AXEL BRANDENBURG¹, MAARIT J. KORPI², AND ANTONY J. MEE³

Received April 11, 2006, accepted September 7, 2006

ABSTRACT

The thermal instability with a piecewise power law cooling function is investigated using one- and three-dimensional simulations with periodic and shearing-periodic boundary conditions in the presence of constant thermal diffusion and kinematic viscosity coefficients. Consistent with earlier findings, the flow behavior depends on the average density, $\langle\rho\rangle$. When $\langle\rho\rangle$ is in the range $(1-5) \times 10^{-24} \text{ g cm}^{-3}$ the system is unstable and segregates into cool and warm phases with temperatures of roughly 100 and 10^4 K , respectively. However, in all cases the resulting average pressure $\langle p\rangle$ is independent of $\langle\rho\rangle$ and just a little above the minimum value. For a constant heating rate of $0.015 \text{ erg g}^{-1} \text{ s}^{-1}$, the mean pressure is around $24 \times 10^{-14} \text{ dyn}$ (corresponding to $p/k_B \approx 1750 \text{ K cm}^{-3}$). Cool patches tend to coalesce into bigger ones. In all cases investigated there is no sustained turbulence, which is in agreement with earlier results. Simulations in which turbulence is driven by a body force show that when rms velocities of between 10 and 30 km/s are obtained, the resulting dissipation rates are comparable to the thermal energy input rate. The resulting mean pressures are then about $30 \times 10^{-14} \text{ dyn}$, corresponding to $p/k_B \approx 2170 \text{ K cm}^{-3}$. This is comparable to the value expected for the Galaxy. Differential rotation tends to make the flow two-dimensional, that is, uniform in the streamwise direction, but this does not lead to instability.

Subject headings: hydrodynamics, instabilities, turbulence, ISM: general

1. INTRODUCTION

The importance of thermal instability (TI) has been extensively studied in the context of the generation and regulation of structures in the atomic interstellar medium (the so-called cold and warm atomic phases usually denoted as CNM and WNM), for a review see e.g. Cox (2005). The core idea was presented by Field et al. (1969, hereafter FGH) in their famous two-phase model: two thermally stable phases (cold and cloudy; warm and diffuse) co-exist in pressure equilibrium regulated by the presence of a thermally unstable phase at an intermediate temperature. After the observational determination of the existence of significant amounts of hot gas in the Galaxy, the FGH model was complemented with a third, hot, phase by McKee & Ostriker (1977), in which model most of interstellar space was occupied by million-kelvin gas produced in supernova explosions. Since then, the estimates of the filling factor of the hot component have reduced to 10%–30% near the Galactic midplane, being larger at larger heights. Moreover, most of the hot gas seems to be confined in large bubbles created by clustered supernova activity rather being distributed homogeneously around the Galaxy. In this light, therefore, it seems justified to neglect the hot component and return to the simpler FGH picture when modeling the colder and denser phases of the interstellar medium (ISM).

There have been a number of numerical investigations of the interaction of turbulence and TI. In most papers the turbulence is forced by sources other than the TI itself: random turbulent forcing at varying scales and

Mach numbers (e.g. Gazol et al. 2005), localized injections of energy mimicking stellar winds (e.g. Vázquez-Semadeni et al. 2000), the magnetorotational instability (e.g. Piontek & Ostriker 2005), and systematic large-scale motions such as propagating shock fronts (e.g. Koyama & Inutsuka 2002) and converging flows (Audit & Hennebelle 2005) have been considered. One of the major findings from these models is that, because of the turbulence present in the system, large pressure deviations are generated and significant amounts of gas can exist in the thermally unstable regime. These results suggest that the FGH picture of the ISM exhibiting “discrete” temperatures and densities and a unique equilibrium pressure should be modified in the direction of a “continuum” of states with an overall pressure balance but with large deviations from it.

In recent years the possibility of driving turbulence by the TI itself has received some revived attention. Contrary to Kritsuk & Norman (2002a), who found turbulence to die out as a power law, Koyama & Inutsuka (2006) find the turbulence to be sustained—at least for times up to 0.1 Gyr. The possibility of TI-induced turbulence is potentially similar to the Jeans instability in a self-gravitating medium that is able to maintain a statistically steady state in which the instability drives the turbulence and turbulent heating prevents the disk from cooling into a static equilibrium. Simulations by Gammie (2001) have shown that such a state of self-sustained “gravito-turbulence” is indeed possible. Wada et al. (2000) found a similar result for the case of the combined action of gravitational and thermal instabilities. The possibility of driving turbulence by means of instabilities is indeed quite common in astrophysics. Especially popular is the magneto-rotational instability that is known to drive turbulence in disks (Hawley et al. 1995, Brandenburg et al. 1995), but there is also the Rayleigh-

¹ NORDITA, Copenhagen, Denmark and AlbaNova University Center, Stockholm, Sweden

² Observatory, University of Helsinki, Finland

³ School of Mathematics and Statistics, University of Newcastle, Newcastle upon Tyne, UK

Revision: 1.116 (May 25, 2018)

Benard instability, which leads to turbulent convection (e.g., Kerr 1996).

In this paper we focus on the interaction between turbulence and the nonlinear stages of the TI, starting from one-dimensional calculations and extending them to three dimensions. Following an approach similar to those of Koyama & Inutsuka (2004) and Piontek & Ostriker (2005), we include thermal conduction, which stabilizes the gas at wavelengths smaller than the critical wavenumber of the condensation mode (Field 1965). This wavelength is usually referred to as the the Field length; it allows the structures generated by the TI to be resolved by the chosen numerical grid. Other approaches have also been used: In the model of Sánchez-Salcedo et al. (2002), a nonuniform grid was used to resolve all the scales down to the cooling length, but nevertheless the required amount of gridpoints restricted the calculations to one dimension. In some models (e.g., Gazol et al. 2005), no bulk viscosity or thermal conduction is used, but they are replaced by local resolution-dependent artificial viscosities damping Nyquist-scale unresolvable structures.

2. MODEL

2.1. Governing equations

We consider the governing equations for a compressible perfect gas,

$$\frac{D \ln \rho}{Dt} = -\nabla \cdot \mathbf{u}, \quad (1)$$

$$\rho \frac{D\mathbf{u}}{Dt} = -\nabla p + \nabla \cdot (2\nu\rho\mathbf{S}), \quad (2)$$

$$T \frac{Ds}{Dt} = 2\nu\mathbf{S}^2 + \frac{1}{\rho} \nabla \cdot (c_p \rho \chi \nabla T) - \mathcal{L}, \quad (3)$$

where \mathbf{u} is the velocity, ρ is the density, s is the specific entropy, with $S_{ij} = \frac{1}{2}(u_{i,j} + u_{j,i}) - \frac{1}{3}\delta_{ij} \nabla \cdot \mathbf{u}$ being the traceless rate of strain tensor, ν is the kinematic viscosity, χ is the thermal diffusivity, and \mathcal{L} is the net cooling or heating, that is, the difference between cooling and heating functions, with

$$\mathcal{L} = \rho\Lambda - \Gamma, \quad (4)$$

where $\Gamma = \text{const}$ is assumed for the heating function. Here we consider the photoelectric heating by interstellar grains caused by the stellar UV radiation field, for which Wolfire et al. (1995) give a value of $0.015 \text{ erg g}^{-1} \text{ s}^{-1}$ at $n = 1 \text{ cm}^{-3}$.

Following common practice, we adopt a perfect gas for which ρ and s are related to pressure p and temperature T by the relations

$$p = \frac{\mathcal{R}}{\mu} \rho T, \quad s = c_v \ln p - c_p \ln \rho + s_0, \quad (5)$$

where $\mathcal{R} = 8.314 \times 10^7 \text{ cm}^2 \text{ s}^{-2} \text{ K}^{-1}$ is the universal gas constant, μ is the mean molecular weight (here we assume $\mu = 0.62$ in all cases and neglect the effects of partial ionization), and $\mathcal{R}/\mu = c_p - c_v$, with c_p and c_v being the specific heats at constant pressure and volume, respectively; $\gamma = c_p/c_v = 5/3$ is their assumed ratio. The adiabatic sound speed c_s and the temperature are

TABLE 1
COEFFICIENTS FOR THE COOLING CURVE GIVEN BY EQ. (6).

i	T_i	$C_{i,i+1}$	$\beta_{i,i+1}$
1	10	3.70×10^{16}	2.12
2	141	9.46×10^{18}	1.00
3	313	1.185×10^{20}	0.56
4	6102	2×10^8	3.67
5	10^5	7.96×10^{29}	-0.65

related to the other quantities via $c_s^2 = \gamma \mathcal{R} T / \mu$. The specific entropy is defined up to a constant s_0 , whose value is unimportant for the dynamics.

We adopt a parameterization of the cooling function approximately equal to that given by Sánchez-Salcedo et al. (2002), which has been obtained by fitting a piecewise power law function of the form

$$\Lambda(T) = C_{i,i+1} T^{\beta_{i,i+1}} \quad \text{for } T_i \leq T < T_{i+1}, \quad (6)$$

to the equilibrium pressure curve of the standard model of Wolfire et al. (1995) for the ISM in the solar neighborhood. When thermal equilibrium with the chosen background heating function, Γ is assumed, and a continuity requirement for Λ ,

$$C_{i-1,i} = C_{i,i+1} T_i^{(\beta_{i,i+1} - \beta_{i-1,i})}, \quad (7)$$

is taken into account, we arrive at the values of the coefficients listed in Table 1. The coefficients $C_{i,i+1}$ given by Sánchez-Salcedo et al. (2002) deviate from this condition by 4%–8%. It turned out that with their original coefficients the flow amplitude showed spurious oscillations in time which disappeared when we use the revised coefficients.

It is convenient to measure time in gigayears, speed in kilometers per second, and density in units of $10^{-24} \text{ g cm}^{-3}$. Pressure is therefore measured in units of 10^{-14} dyn . Our unit of length is therefore $1 \text{ (km/s)} \times 1 \text{ Gyr} = 1.02 \text{ kpc}$; in the following, we denote the unit of length for simplicity as 1 kpc, keeping in mind that it should really be 1.02 kpc. Viscosity and thermal diffusivity are measured in units of $\text{Gyr km}^2 \text{ s}^{-2}$.

We use periodic boundary conditions in all three directions for a computational domain of size $(200 \text{ pc})^3$, which is the typical domain size employed in simulations of supernova-driven turbulence in the interstellar medium. However, smaller domains would be more suitable to resolve the smaller scales, as has been done by Kritsuk & Norman (2002a), for example. We use the PENCIL CODE,⁴ which is a non-conservative, high-order, finite-difference code (sixth order in space and third order in time) for solving the compressible hydrodynamic equations. Because of the non-conservative nature of the code, diagnostics giving the total mass and total energy (accounting for heating/cooling terms) are monitored and simulations are only deemed useful if these quantities are in fact conserved to reasonable precision. The mesh spacings in the three directions are assumed to be the same, that is, $\delta x = \delta y = \delta z$.

We emphasize that no shock or hyperviscosity has been used in the present simulation. Therefore, the only

⁴ see <http://www.nordita.dk/software/pencil-code>.

means of stabilizing the code is through regular viscosity ν and thermal diffusivity χ . In order to damp unresolved ripples at the mesh scale δx in a trail of structures moving at speed U , the minimum viscosity and minimum diffusion must be on the order of $0.01 U \delta x$ (see Brandenburg & Dobler 2002). In all our simulations the velocities are subsonic, so the fastest pattern speed is given by the sound speed. In the following we quote the mesh Reynolds number based on the mean (volume averaged) sound speed, \bar{c}_s , and the mesh size δx ,

$$\text{Re}_{\text{mesh}} = \bar{c}_s \delta x / \nu, \quad (8)$$

The minimum viscosity quoted above corresponds to a largest permissible value of Re_{mesh} of about 100. However, in the presence of strong converging flows and shocks the largest permissible value may be of order unity.

Since we want to use minimal values for ν and χ in both the warm and cold components we keep ν and χ constant rather than, for example, the dynamical viscosity or the quantity $\mathcal{K} \equiv \rho \gamma \chi$ (see, e.g., Piontek & Ostriker 2004). In the latter case, χ would vary by 2 orders of magnitude between warm and cold phases. If the mesh were sufficiently fine, one could allow for a physically motivated dependence of χ on T , but this is neglected here.

In the calculations, we have adopted two different values of ν and χ (5×10^{-3} and 5×10^{-4} Gyr km² s⁻²), keeping their ratio, the Prandtl number $\text{Pr} = \nu/\chi$, fixed to unity. The corresponding Field lengths, calculated from equation (12) using the initial cooling timescale of approximately 1 Myr, are 24 and 7.7 pc, respectively. Compared with the average value of the thermal diffusion in the neutral ISM, roughly 6×10^{20} cm² s⁻¹ $\approx 2 \times 10^{-6}$ Gyr km² s⁻², corresponding to a Field length of about 0.5 pc, the adopted values are larger by 2–4 orders of magnitude. The cooling length $l_{\text{cool}} \approx \tau_{\text{cool}} u_{\text{rms}}$ is close to the physical Field length, being roughly 0.4 pc. Our chosen values of χ due to the preference of a large domain size, are therefore too large to resolve the fine structure in the accretion fronts that result from the cooling process. This is a similar setup to the one investigated by Piontek & Ostriker (2004, 2005); models achieving Field lengths smaller than the cooling length include for example, Sánchez-Salcedo et al. (2001), Kritsuk & Norman (2004), and Koyama & Inutsuka (2004).

2.2. Stability properties

The first thorough stability analysis was done by Field (1965), who also included the stabilizing effect of thermal diffusion. Assuming the solutions to be proportional to $\exp(nt + i\mathbf{k} \cdot \mathbf{x})$, the dispersion relation can be written in the form

$$n(n + n_\nu)(n + \beta n_\rho + n_\chi) + \omega_{\text{ac}}^2 \left[n + \frac{(\beta - 1)n_\rho + n_\chi}{\gamma} \right] = 0, \quad (9)$$

where we have also included the effect of kinematic viscosity. Here, $\omega_{\text{ac}} = c_s k$ is the acoustic frequency and $\beta = d \ln \Lambda / d \ln T$ is the local logarithmic slope of the cooling function. We have restricted ourselves to cases where Γ is constant and Λ depends only on T . The cooling time is characterized by the quantity

$$n_\rho = \rho_0 \mathcal{L}_\rho / (c_v T), \quad (10)$$

which is to be evaluated for the equilibrium solution. Here, $\mathcal{L}_\rho = (\partial \mathcal{L} / \partial \rho)_T = \Lambda$. Note that n_ρ is just the inverse cooling time defined by Piontek & Ostriker (2004). The subscript ρ follows from a similar notation used by Field (1965) who defined instead a wavenumber $k_\rho = n_\rho / c_s$, which is also referred to as the cooling wavenumber. Viscous and diffusive effects are characterized by the corresponding rates,

$$n_\nu = \frac{4}{3} \nu k^2, \quad n_\chi = \gamma \chi k^2. \quad (11)$$

Thermal instability is only possible for $\beta < 1$. This condition corresponds to the isobaric instability criterion of Field (1965). The isochoric and isentropic criteria, $\beta < 0$ and $\beta < -1/(\gamma - 1) = -3/2$, respectively, are less strict in that the isobaric criterion for instability is then automatically satisfied.

When thermal diffusivity is included, the gas can be stabilized (even though $\beta < 1$) provided the largest possible wavenumber in the system (which we denote as k_1) is larger than the Field wavenumber, k_F , defined as

$$k_F^2 = (1 - \beta)n_\rho / (\gamma \chi) \quad (\text{for } \beta < 1). \quad (12)$$

The instability has therefore the character of an ordinary long-wave instability requiring $k_1 < k_F$. The corresponding dispersion relation is shown in Figure 1 for various values of n_ρ using $\nu = \chi$ (top) and $\nu = 0$ (bottom). The value of χ is given in terms of the ratio $n_\rho / (c_s k_F)$, for which three values have been chosen to illustrate this dependence. As expected, the presence of kinematic viscosity has a stabilizing effect. Setting $\nu = 0$ leads to somewhat larger growth rates, especially when $n_\rho / (c_s k_F)$ is large and $n / (c_s k_F)$ is small. For $n_\rho / (c_s k_F) = 2$, for example, the normalized growth rate for $\nu = \chi$ is the largest among the three cases shown in Figure 1, but it hardly increases when $\nu \rightarrow 0$, in which case the growth rate is actually the smallest among the three cases.

In the limit $k \ll k_F$, which is relevant when diffusive effects are negligible, the unstable branch of the dispersion relation reduces to

$$n = c_{\text{iso}} k \sqrt{\beta^{-1} - 1}, \quad (13)$$

where we have introduced the isothermal sound speed, $c_{\text{iso}} \equiv c_s / \sqrt{\gamma}$. Note that in the thermally stable case with $\beta \gg 1$ we obtain the usual dispersion relation for isothermal sound waves, $\omega = c_{\text{iso}} k$, where $\omega = in$ is the frequency. For $\beta = 1/2$ this approximation yields $n = c_{\text{iso}} k$, as stated by Field (1965) in his equation (36). For $\beta = 0.56$ this approximation is shown in Figure 1 as a straight dash-dotted line.

2.3. Saturation properties

In the absence of thermal diffusion, thermal equilibrium is given by the condition $\mathcal{L} = 0$. Pressure equilibrium between the cold and warm phases requires that equilibrium is achieved under the constraint of constant pressure. Such an equilibrium would however only be stable if a temperature increase would lead to correspondingly more cooling, that is, if

$$\left(\frac{\partial \mathcal{L}}{\partial T} \right)_p > 0, \quad (\text{stability}). \quad (14)$$

where the subscript p indicates that the pressure is held constant. In Figure 2 we plot \mathcal{L} as a function of T for

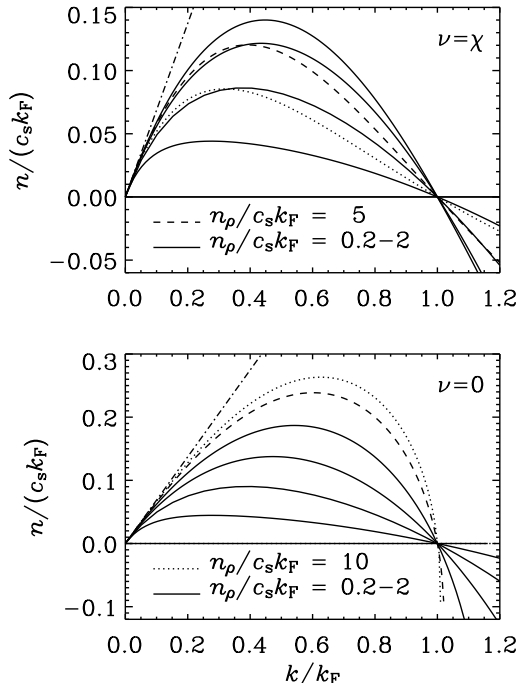


FIG. 1.— Dispersion relation $n(k)$ in the unstable regime with $\beta = 0.56$, obtained by solving eq. (9) for a representative range of values of $n_\rho/c_s k_F$. The $n(k)$ curves are normalized in terms of k_F and $c_s k_F$. In the range $n_\rho/c_s k_F = 0.2-2$ (solid lines) the maxima of $n/(c_s k_F)$ are monotonically increasing. The curves for $n_\rho/c_s k_F = 5$ (dashed line) and $n_\rho/c_s k_F = 10$ (dotted line) deviate from this trend. The diagonal dash-dotted line indicates the approximation valid for small wavenumbers [eq. (13)].

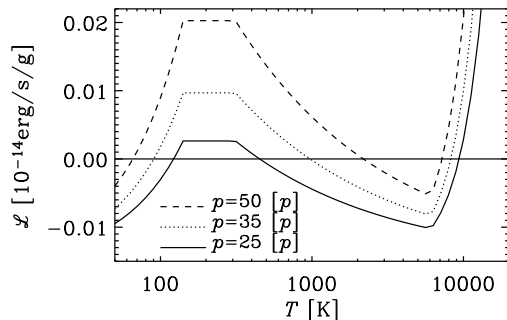


FIG. 2.— Net cooling vs. temperature for three values of p , given in units of $[p] = 10^{-14}$ dyn.

constant p ; three values are considered: $p = 25, 35$, and 50 , all in units of $[p] \equiv 10^{-14}$ dyn. This figure shows that there can be two stable states at about 10^2 and 10^4 K. We denote these values by T_C and T_W for the cold and warm phases. At $T \approx 10^3$ K there is an unstable equilibrium, whose temperature is denoted T_U . The densities of the three equilibria, obtained by solving $\mathcal{L}(T; p) = 0$ for T numerically for given p and then expressing the result in terms of $\rho = \rho(T, p)$, are plotted in Figure 3.

When setting up a simulation the density is particularly useful, because its mean value in a certain volume is proportional to the mass, which is constant for closed and periodic boundary conditions, such as those consid-

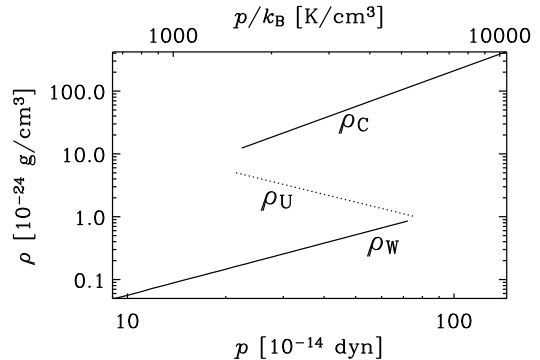


FIG. 3.— The two stable solution branches, ρ_C and ρ_W (solid lines), and the unstable solution branch, ρ_U (dotted line), as a function of p . On the top the pressure is normalized by the Boltzmann constant, p/k_B .

ered here. Thus, one can ask the question what is the resulting mean pressure as a function of the mean density. Of course, as long as the gas is thermally stable, the density will be uniform and hence its mean value is always equal to the actual value at any point, so it is given by combining the equation of state with the condition of thermal equilibrium. As is evident from Figure 3, when the density is in the range $(1-5) \times 10^{-24}$ g cm 3 , there is no stable solution. This means that the gas will fragment into cold patches of temperature $T = T_C$ with density ρ_C , and the rest of the ambient gas warms up to the stable solution branch $T = T_W$ with density ρ_W . As a direct result of mass conservation in our periodic domain, the filling factor of the cold component can be expressed in terms of the mean density, $\langle \rho \rangle$, which is known from the initial condition. Using the definition of the filling factor,

$$f \rho_C + (1 - f) \rho_W = \langle \rho \rangle, \quad (15)$$

the value of f is given by

$$f = \frac{\langle \rho \rangle - \rho_W}{\rho_C - \rho_W}. \quad (16)$$

A similar analysis can also be adopted for calculating $\langle T \rangle$. This allows us to calculate the correlation coefficient ϵ in the relation

$$\langle \rho T \rangle = \epsilon \langle \rho \rangle \langle T \rangle \quad (17)$$

where

$$\epsilon \approx \frac{1}{f(1-f)} \frac{T_W}{T_C} \approx \frac{0.013}{f(1-f)}. \quad (18)$$

The correlation coefficient is small because $\langle \rho T \rangle$ decreases slightly and $\langle \rho \rangle \langle T \rangle$ increases strongly as the system segregates, as demonstrated below (in connection with Figure 4). The expression $\langle \rho \rangle \langle T \rangle$ is almost entirely determined by the product of the volume-weighted density (or relative mass) in the cold phase, $f \rho_C$, and the volume weighted temperature in the warm phase, $(1-f) T_W$, so both factors are large compared with their respective average values.

The segregation phenomenon has already been studied in a one-dimensional model (Sánchez-Salcedo et al. 2002). Here, except for an additional perturbation, the initial condition is assumed uniform, $\rho = \rho_0 \equiv \langle \rho \rangle$, and the value of ρ_0 is varied between different simulations.

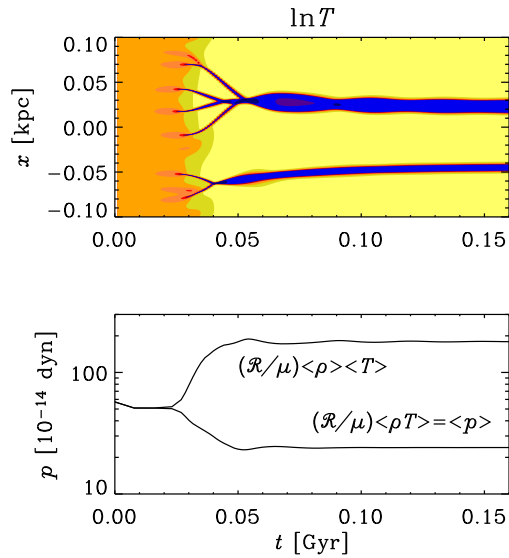


FIG. 4.— Evolution of $\ln T$ in a space-time diagram (top) and of the mean pressure (bottom) in a one-dimensional simulation with 1024 mesh points and $\nu = \chi = 5 \times 10^{-4} \text{ Gyr km}^2 \text{ s}^{-2}$. During early times, the rms velocity grows exponentially at a rate of about 220 Gyr^{-1} .

In all the runs presented below the initial perturbation is gaussian noise with an rms fluctuation amplitude of $10^{-26} \text{ g cm}^{-3}$. When ρ_0 (in units of $10^{-24} \text{ g cm}^{-3}$) is between 0.96 and 5.1, the gas is thermally unstable and segregates into cold and warm components. As time goes on, some of the cold spots may move because of slight pressure imbalance until they coalesce into bigger fragments. This coalescence was also found by Sánchez-Salcedo et al. (2002) and Koyama & Inutsuka (2004).

In Figure 4 we plot the evolution of $\ln T$ in a space-time diagram (top) and that of the mean pressure in a one-dimensional simulation. Here, $\nu = \chi = 5 \times 10^{-4} \text{ Gyr km}^2 \text{ s}^{-2}$ which, together with the initial values of $c_s = 7.5 \text{ km/s}$ and $n_\rho = 980 \text{ Gyr}^{-1}$, yields $k_F = 720 \text{ kpc}^{-1} = 23k_1$, and hence $n_\rho/(c_s k_F) \approx 0.2$.

During early times the rms velocity grows exponentially at a rate of about 210 Gyr^{-1} , which is consistent with the peak value of $n/(c_s k_F) \approx 0.04$ for our set of parameters. Note that the mean pressure settles around $24 \times 10^{-14} \text{ dyn}$ once the instability has saturated. At that time, smaller structures may still coalesce into larger ones, but the total filling factor remains approximately constant. During the evolution away from the unstable homogeneous state, the mean pressure (proportional to $\langle \rho T \rangle$) decreases by about a factor of 2, but the product $\langle \rho \rangle \langle T \rangle$ increases by almost a factor of 4. When ρ_0 is between 5.2 and 11 (in units of $10^{-24} \text{ g cm}^{-3}$) the gas is marginally stable ($\beta = 1$; see Table 1), so in that range there will be no segregation into different phases.

When the mean density is outside the range between 0.96 and 5.1 (in units of $10^{-24} \text{ g cm}^{-3}$), the gas is thermally stable and remains uniform. The dependence of the pressure on the density can be obtained in parametric form by calculating, using temperature as a parameter, $\rho(T)$ and $p(T)$, that is,

$$\rho(T) = \frac{\Gamma}{\Lambda(T)}, \quad p(T) = \frac{\mathcal{R}T}{\mu} \frac{\Gamma}{\Lambda(T)}, \quad (19)$$

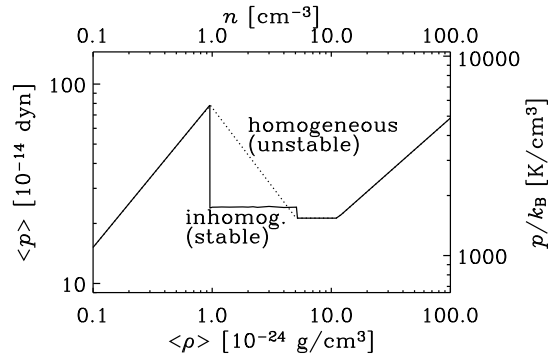


FIG. 5.— Mean pressure vs. mean density in a one-dimensional simulation (solid line), compared with the values obtained for a homogeneous system (dotted line). The dotted line (which agrees with the solid line in the stable regime and hence cannot be seen there) was obtained by plotting $p(T)$ vs. $\rho(T)$ using T as a parameter in eq. (19). On the right axis, the pressure is normalized by the Boltzmann constant, p/k_B , and at the top the number density is given. The simulation has 128 mesh points and $\nu = \chi = 5 \times 10^{-3} \text{ Gyr km}^2 \text{ s}^{-2}$.

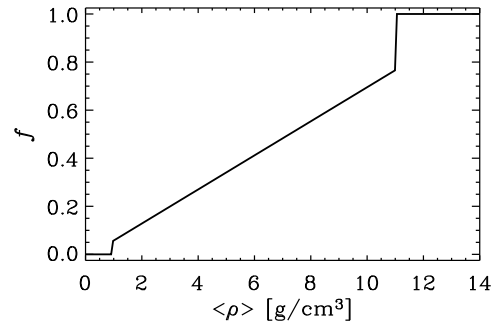


FIG. 6.— Filling factor f as a function of the mean density, as predicted by eq. (16).

and plotting the two against each other (see Figure 5, dotted line). The numerically obtained values for the mean pressure $\langle p \rangle$, for different mean densities $\langle \rho \rangle$, agree with those obtained under the assumption of homogeneity.

In the unstable regime the pressure is, surprisingly, independent of $\langle \rho \rangle$, and always around $\langle p \rangle \approx 24.2 \times 10^{-14} \text{ dyn}$. (Figure 5 shows slight variations about this value; this is probably a consequence of the fact that the coefficients $C_{i,i+1}$ are only implemented up to three to four significant figures, so the cooling curve is still not perfectly continuous.) Figure 3 shows that for $\langle p \rangle \approx 24.2 \times 10^{-14} \text{ dyn}$ the warm and cool phases have $\rho_w \approx 0.19$ and $\rho_c \approx 14.3$, respectively. This allows us to determine the filling factor as a function of $\langle \rho \rangle$; see Figure 6. In most of the runs considered below we expect $\langle \rho \rangle = 2$, so $f \approx 13\%$. In practice we estimate the filling factor as the fraction of mesh points for which $T < T_U$, where $T_U \approx 420 \text{ K}$ (corresponding to $\rho_U = 4.3 \times 10^{-24} \text{ g cm}^{-3}$ in Figure 3) for $\langle p \rangle = 24.2 \times 10^{-14} \text{ dyn}$. The filling factors determined in this way are quoted for the simulations presented below.

There is a tendency for cool patches to travel and to

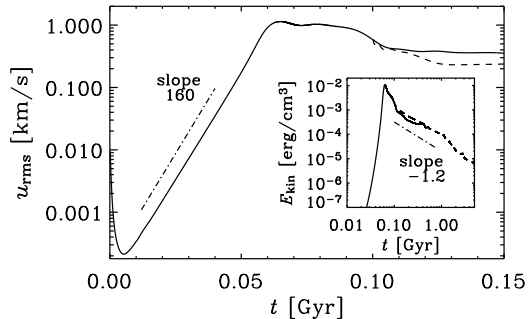


FIG. 7.— The rms velocity and kinetic energy for a three-dimensional run with $\nu = \chi = 5 \times 10^{-3} \text{ Gyr km}^2 \text{ s}^{-2}$ and 256³ mesh points. The dashed line represents a solution with $\nu = \chi = 5 \times 10^{-4} \text{ Gyr km}^2 \text{ s}^{-2}$, which was restarted at $t = 0.1 \text{ Gyr}$ from a run with 10 times higher viscosity. Here $\langle \rho \rangle \approx 1.7 \times 10^{-24} \text{ g cm}^{-3}$, $\langle p \rangle \approx 24.3 \times 10^{-14} \text{ dyn}$, and $\langle T \rangle \approx 8200 \text{ K}$.

coalesce into bigger ones (see, e.g., Sánchez-Salcedo et al. 2002). This property is reminiscent of earlier work in the context of the thermal instability. Elphick et al. (1991, 1992) found traveling front solutions and also the merging of smaller patches into bigger ones, which they associate loosely with an inverse cascade behavior. However, in their work they only discuss the energy equation and not dynamical processes. In the case they discuss the kink and antikink fronts always travel toward or away from each other, thus resulting in the annihilation and creation of denser clouds. This is not seen in the present work. Also, they discuss much smaller objects of size $\sim 0.02 \text{ pc}$ which have considerably shorter sound crossing times. Furthermore, early on in their evolution our clouds tend to accelerate toward each other, as can be seen from the curved trajectories.

3. THREE-DIMENSIONAL SIMULATIONS

3.1. Fully periodic boundary conditions

In this section we discuss the results of three-dimensional simulations. The basic properties of the one-dimensional simulations, presented in §2.3, carry over to the three-dimensional regime. As expected, the growth rates are the same as those found in the one-dimensional case. The resulting mean pressure $\langle p \rangle$ and hence the filling factor, as given by eq. (16), are also quite similar to those of the one-dimensional case. Nevertheless, even though significant amounts of turbulent heating are being produced at the most violent phase of the instability, there is in our cases always a subsequent relaxation phase in which the flow speed tends to vanish on a long time scale (see Figure 7). This agrees with earlier findings of Kritsuk & Norman (2002a). The energy decay is consistent with a $t^{-1.2}$ law, just like in ordinary turbulence (e.g. Mac Low et al. 1998, Haugen & Brandenburg 2004). This is also consistent with the results of Kritsuk & Norman (2002a), who reported decay exponents in the range 1–2 for box sizes between 5 and 500 pc using also a more detailed cooling curve in tabular form. On the other hand, Koyama & Inutsuka (2006) find that turbulence remains self-sustained for times up to 0.1 Gyr.

We emphasize again that we have used constant kinematic viscosity and constant thermal diffusivity in our

simulations. For the runs shown in Figs 7–13 we have used $\nu = \chi = 5 \times 10^{-3} \text{ Gyr km}^2 \text{ s}^{-2}$ until $t = 0.1 \text{ Gyr}$ (corresponding to $\text{Re}_{\text{mesh}} = 2$). This corresponds to $k_F = 230 \text{ kpc}^{-1} = 23k_1$, and hence $n_\rho/(c_s k_F) \approx 0.6$, so the initial growth rate is 160 Gyr^{-1} . This is again consistent with Figure 4 yielding a peak value of $n/(c_s k_F) \approx 0.09$ for our set of parameters.

However, after having reached the peak velocity, the flow has become sufficiently quiescent so that it is possible to decrease the viscosity by a factor of about 10, corresponding to $\text{Re}_{\text{mesh}} = 20$. Figure 8 shows images of $\ln T$ on the periphery of the simulation domain at a few selected times after having lowered the viscosity and thermal viscosity. Animations of temperature and density⁵ show that late in the simulation, cold patches of gas are still moving about, but this is presumably just a response to small-amplitude, small wavenumber variations in overall pressure requiring a much longer time scale to equilibrate.

During the course of the simulation the value of k_F (based on the averaged value of n_ρ) increases between the initial value before saturation of the instability ($k_F \delta x \approx 0.2$) and the saturated state ($k_F \delta x \approx 1$ with the higher viscosity and $k_F \delta x \approx 3$ with the lower viscosity). At the end of the simulation the gas is sharply segregated into warm and cool phases in almost perfect pressure equilibrium. This can be seen clearly from probability density functions of the various quantities that are discussed in §3.3.

3.2. Shearing-periodic boundary conditions

The shearing sheet approximation simulates the local conditions in a disk with strong radial differential rotation in the limit of large radii. Curvature can thus be neglected and the shear can be assumed linear in radius, so that we only have an underlying linear shear flow $\mathbf{U}_0 = (0, Sx, 0)^T$, where S is constant. The Coriolis force, $2\boldsymbol{\Omega} \times \mathbf{u}$ is added, where $\boldsymbol{\Omega} = (0, 0, \Omega)$ is the angular velocity vector. It is assumed that S scales with the angular velocity, so here we take $S = -\Omega$ which is appropriate for galactic disks with a constant linear velocity law. The combined effects of shear and Coriolis force can be subsumed into a single vector (Brandenburg et al. 1995),

$$\mathbf{f}(\mathbf{u}) = \begin{pmatrix} 2\Omega u_y \\ -(2\Omega + S)u_x \\ 0 \end{pmatrix}, \quad (20)$$

which is then added on the right hand side of eq. (2). After this modification the velocity \mathbf{u} describes the deviation from the shear flow and does thus not include the basic shear. The basic shear flow appears still explicitly as an additional advection operator of the form $\mathbf{U}_0 \cdot \nabla = Sx\partial_y$.

In the following we consider the case $\Omega = 100 \text{ Gyr}^{-1}$, but we have also considered the case $\Omega = 25 \text{ Gyr}^{-1}$ (appropriate for our Galaxy). The difference between the two simulations is small. The main thing that happens in all these simulations is a tendency for the flow to become sheared out, so any variations in the streamwise

⁵ see http://www.nordita.dk/brandenb/movies/thermal_inst.

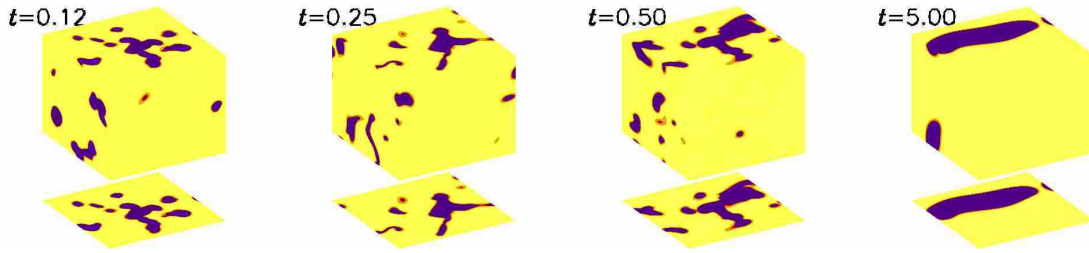


FIG. 8.— Visualization of $\ln T$ on the periphery of the box at different times, for $\nu = \chi = 5 \times 10^{-4} \text{ Gyr km}^2 \text{ s}^{-2}$ with 256^3 mesh points. $\langle \rho \rangle \approx 1.7 \times 10^{-24} \text{ g cm}^{-3}$, $\langle p \rangle \approx 24.3 \times 10^{-14} \text{ dyn}$, $\langle T \rangle \approx 8200 \text{ K}$, and $f = 11\%$. For this run $k_F/k_1 = 130$ and $n_\rho/(c_s k_F) = 0.37$. Prior to $t = 0.1 \text{ Gyr}$, both viscosity and thermal diffusivity were 10 times larger; $\nu = \chi = 5 \times 10^{-3} \text{ Gyr km}^2 \text{ s}^{-2}$ with $k_F/k_1 = 41$ and $n_\rho/(c_s k_F) = 1.2$. The growth rate is about 160 Gyr^{-1} . Note the isolated cool patches (dark shaded) compared with the extended warm background (light shades). As time goes on, the dark patches merge with each other and grow.

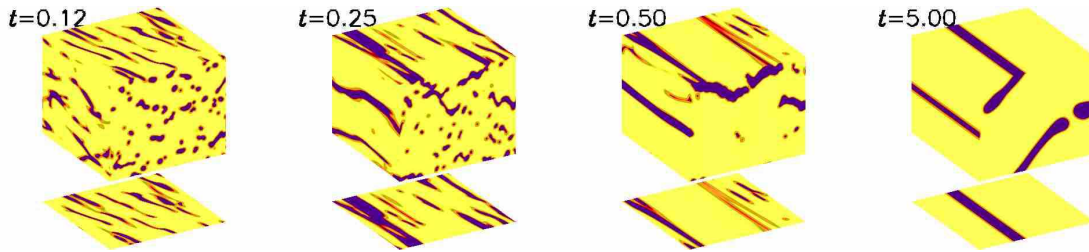


FIG. 9.— Visualization of $\ln T$ on the periphery of the box at different times, for $\nu = \chi = 5 \times 10^{-4} \text{ Gyr km}^2 \text{ s}^{-2}$ and 256^3 mesh points. $\langle \rho \rangle \approx 1.74 \times 10^{-24} \text{ g cm}^{-3}$, $\langle p \rangle \approx 24.2 \times 10^{-14} \text{ dyn}$, and $\langle T \rangle \approx 8200 \text{ K}$. Here $\Omega = 100 \text{ Gyr}^{-1}$ and $S = -\Omega$. For this run $k_F/k_1 = 32$ and $n_\rho/(c_s k_F) = 1.5$. The growth rate is about 190 Gyr^{-1} , which is somewhat larger than for the corresponding non-shearing run. Note that the initially produced structures are quickly sheared out.

direction become sheared out and the flow becomes essentially two-dimensional; see Figure 9. However, shear does not seem to lead to instability, even though the kinematic growth rate of the thermal instability is apparently somewhat increased (190 Gyr^{-1} instead of 160 Gyr^{-1}). This absence of sustained turbulence is somewhat disappointing, because one might have hoped that the thermal instability would have led to condensation in the streamwise direction and thus to new structures that could then be sheared out again. This seems to be prevented by the general tendency of coalescence, preventing breakup into new structures in the streamwise direction. However, it may still be interesting to reconsider this issue in the future at significantly higher resolution and larger Reynolds number.

3.3. Forced simulations

Given that the TI did not produce sustained turbulent flows, we consider now cases which turbulence is driven by an additional body force in the momentum equation. We consider here a forcing function consisting of plane waves whose wavevector is chosen randomly at each time step and has length between 2.5 and 3.5 times the smallest wavenumber in the box, $k_1 = 2\pi/(0.2 \text{ kpc})$. This forcing function is therefore δ -correlated in time and approximately monochromatic in space (see also Sánchez-Salcedo et al. [2002] for simulations in one dimension).

It turns out that when the flow is driven sufficiently strongly to produce rms velocities of around $10\text{--}30 \text{ km/s}$, the turbulent energy that is dissipated into heat is only about comparable to the energy needed to balance the losses from cooling (see Figure 10). The mean pressure is increased slightly to about $30 \times 10^{-14} \text{ dyn}$, corresponding to $p/k_B \approx 2170 \text{ K cm}^{-3}$. In both cases the spectra of \mathbf{u} (kinetic energy) and ρ (density) are similar, except

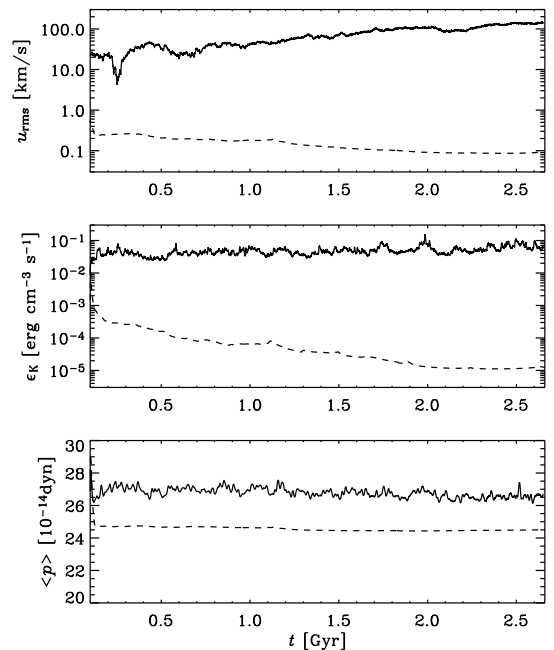


FIG. 10.— Comparison of the rms velocity (top), dissipation rate ϵ_K (middle), and mean pressure (bottom), for a forced simulation (solid lines) and a nonforced simulation (dotted lines); same run as in Figure 8). Both cases have $\nu = \chi = 5 \times 10^{-4} \text{ Gyr km}^2 \text{ s}^{-2}$ and 256^3 mesh points.

that the unforced run shows more relative power in the density spectra at large scales; see Figure 11. Over a small range of wavenumbers the local slope of the kinetic energy spectra is around $-5/3$. By comparison, Kritsuk & Norman (2004) found shallower spectra with spectral slope close to -1 in their decaying simulations with TI,

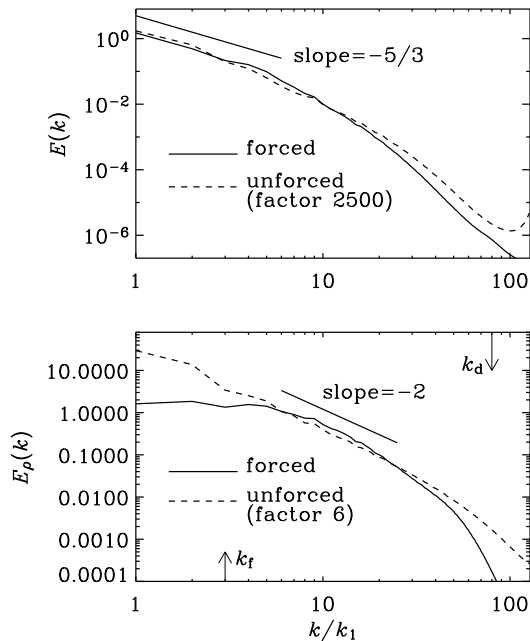


FIG. 11.— Comparison of time-averaged kinetic energy spectra (top) and density spectra (bottom) for the forced and unforced runs shown in Figure 10. The kinetic energy and density spectra for the unforced case are scaled so as to make them overlap at intermediate wavenumbers. For the forced run the forcing wavenumber, $k_f = 2.5k_1$, is indicated, while the dissipation wavenumber, $k_d = (\omega_{\text{rms}}/\nu)^{1/2}$, is shown for the unforced run.

but this could be a feature of the numerical dissipation used in their code. The dissipation wavenumber, $k_d = (\omega_{\text{rms}}/\nu)^{1/2}$, where ω_{rms} is the rms of the vorticity, $\boldsymbol{\omega} = \nabla \times \mathbf{u}$ is shown for the unforced run. For the forced run the adopted viscosity is critically low, as evidenced by the small rise in the kinetic energy at large wavenumbers. In fact, the dissipation scale for this run is just outside the plot range. It is perhaps because of the presence of cooling, which contributes to energy removal, that this run has still been successful.

As in the unforced case, the gas is segregated into warm and cool phases, but now they are only in *approximate* pressure equilibrium; in Figure 12, we show probability density functions (PDFs) of $\ln \rho$, $\ln T$, and $\ln p$. The turbulent increase of the mean pressure has only a small effect on the preferred temperatures in the warm and cold phases, whereas the density peaks are shifted toward higher densities, as expected if the system were still following the equilibrium pressure-density relation. The turbulence forced at relatively small scales has the most drastic effect on the cold cloudy component, the distribution of which has become significantly wider while the high density wing was developing. The maximum density in the forced case is roughly an order of magnitude larger than in the pure TI case. A similar wing is observed at low temperatures, reaching values down to the cooling cut-off of 10 K in the highest density regions. While in the pure TI case the pressure in the saturated state shows a very narrow distribution around the mean, in the forced cases the distribution is broad with extrema that vary by almost 1 order of magnitude. In addition to this broadening of the pressure distribution already pointed out in several previous studies (e.g. Gazol et al.

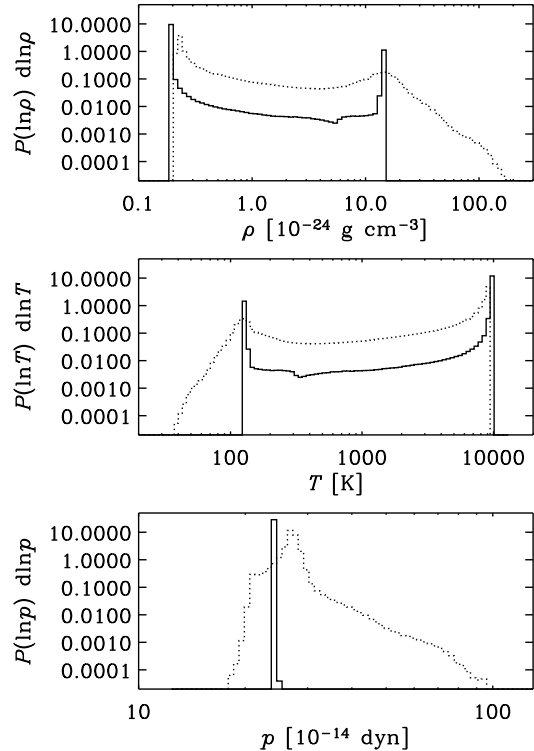


FIG. 12.— Comparison of the probability density functions of $\ln \rho$, $\ln T$, and $\ln p$ at the last snapshot for forced (dotted lines) and unforced (solid lines) cases.

2005), the amount of gas in the “forbidden” (thermally unstable) regime has been observed to increase; in our calculations this is seen as a systematic increase of the level of the PDFs in between the two preferred states, while the peaks themselves become less pronounced. In the forced case, about 6% of the gas is found in the unstable range where ρ is between 1 and 5 times $10^{-24} \text{ g cm}^{-3}$. In the pure TI case, on the other hand, only 2% is in this range. In addition there is a significant fraction of cold high-density overpressured gas that is in the thermally stable regime. Nevertheless, even in the highly turbulent regime the signatures of pure TI are still clearly visible in the density and temperature PDFs (better for warm, worse for cold); the pressure PDF develops broad wings, as is familiar from supernova-driven turbulence simulations (e.g., Korpi et al. 1999; Mac Low et al. 2005), and some earlier TI simulations with forced turbulence (e.g. Gazol et al. 2005). Still, the mean pressure determines the preferred densities and temperatures in the warm and cold phases as though the system followed the equilibrium pressure-density relation.

It is customary to discuss scatter plots of pressure versus density (Sánchez-Salcedo et al. 2002; Piontek & Ostriker 2004, 2005), which allow one to discuss the degree to which the gas is locally in equilibrium. In Figure 5 we showed that the mean pressure, that is, averaged over the entire box, is $\approx 24 \times 10^{-14} \text{ dyn}$ when the mean density is in the unstable range, $\langle \rho \rangle = (1-5) \times 10^{-24} \text{ g cm}^{-3}$. It turns out that this result also holds locally, as can be seen from a scatter plot of pressure versus density and, more conveniently, from a two-dimensional PDF (Figure 13) showing the logarithm of the probability density

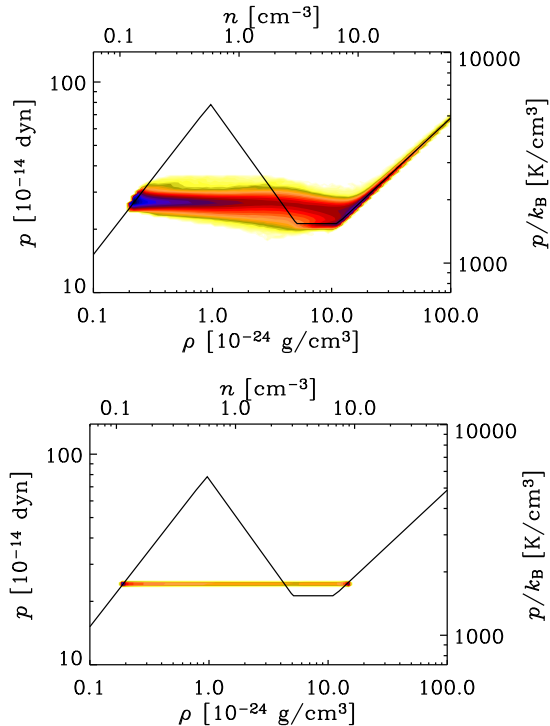


FIG. 13.— Two-dimensional probability density functions of $\ln \rho$ and $\ln p$ for forced (top) and unforced (bottom) simulations. The solid line indicates the thermodynamic equilibrium solution. Dark shades indicate large values of the probability density.

as a function of both $\ln \rho$ and $\ln p$ for both forced and unforced runs. In the unforced case the local pressure is concentrated sharply around 24×10^{-14} dyn over a broad range of local densities, $\rho = 0.2\text{--}20 \times 10^{-24}$ g cm⁻³. In the forced case, the distribution is broadened around the average pressure for $\rho = 0.2\text{--}20 \times 10^{-24}$ g cm⁻³, but there are also dense spots with $\rho \gtrsim 20 \times 10^{-24}$ g cm⁻³ where the gas follows the equilibrium distribution quite sharply, confirming earlier findings of Sánchez-Salcedo et al. (2002) and Piontek & Ostriker (2004, 2005).

4. CONCLUSIONS

Our results confirm the basic findings of Kritsuk & Norman (2002a) in that the TI does not lead to self-sustained turbulence. In the cases considered in this paper the instability just leads to segregation into two different phases, and produces only small velocities in response to the remaining pressure fluctuations. While the growth of the instability occurs over relatively short timescales of a few tens of millions of years, the kinetic energy of these motions decays exponentially with a slope consistent with -1.2 leading to insignificant rms velocities after a few hundred millions of years. Thus, in agreement with Kritsuk & Norman (2002a), the TI alone does not lead to self-sustained turbulence. This is somewhat different from the purely two-dimensional TI cases investigated by Piontek & Ostriker (2004), who report weak (≈ 0.5 km s⁻¹) non-decaying turbulence over timescales of roughly 0.5 Gyr. This behavior seems to carry over into three dimensions (Piontek & Ostriker 2005, see their Fig. 11).

Similar results have also been found recently by

Koyama & Inutsuka (2006), who also include an explicit dynamical viscosity. For times up to 0.1 Gyr their results are nevertheless qualitatively similar to ours in that they also report rms velocities in the range 0.1–0.4 km/s, and their flow topology is similar to ours at early times. They also study smaller box sizes, but their highest turbulence levels occur for their largest box size of $L = 144$ pc, which is similar to ours. In both cases the Field length is about 1/100 of the box size. However, if there is really a difference in sustaining turbulence over long times, then this might be due to a different formulation of thermal conduction which varies here with density, but is constant in the simulations of Piontek & Ostriker (2004, 2005) and Koyama & Inutsuka (2006). In the latter case a constant dynamical viscosity is included, while in our case a constant kinematic viscosity is used. Another difference is the discontinuous nature of the transitions in the previously used cooling function. (The latter was observed to lead to spurious oscillatory motions in some of our preliminary investigations that are not reported here.) However, if the turbulence is real, then this could perhaps be understood as an analogy to the TI-driven turbulence found by Kritsuk & Norman (2002b) in the presence of a time-dependent heating rate. The idea would be that a variable heating rate could perhaps be simulated by introducing nonlinear feedbacks in some of the coefficients.

Another possibility for driving turbulence has been discussed by Murray et al. (1993). They find that a system segregated into two phases by the TI could develop Kelvin-Helmholtz secondary instabilities if cold clouds move at transonic speeds relative to a warm background. They speculate that such motions could be the result of buoyancy forces or some pressure imbalance. However, this scenario does not seem to apply to our simulations where pressure imbalances become quite small at late times. A related possibility would be secondary instabilities caused by differential rotation. Again, in the present simulations this did not occur either. Instead, shear mainly causes the flow to become two-dimensional, that is, uniform in the streamwise direction. However, in the simulations the TI shows no tendency of subsequent fragmentation of structures in the streamwise direction. There might still be some hope that the fragments could be susceptible to a baroclinic instability, but this may require substantially higher resolution than what we have considered in the present paper.

In the pure TI, cases the system develops into a new segregated state in which each phase is stable. The cold patches have a tendency to coalesce into bigger ones that are more resistant to the possibility of breaking up. It is conceivable that the process of coalescence is slowed down when the value of χ is decreased. This might become more plausible when realizing that, because of the thermal instability, the energy equation is essentially of the type of a reaction-diffusion equation. Under the assumption of perfect pressure equilibrium at all times, Elphick et al. (1991) showed that this equation permits traveling kink solutions. If a front were to travel into an unstable equilibrium state, the front speed would be proportional to the square root of the product of diffusivity and the growth rate of the instability. In the present case, however, warm and cold equilibrium states “compete” against each other, so fronts would not propagate. Only in two and three dimensions, where fronts are

in general curved, they tend to be driven diffusively toward the direction of the center of curvature; see Shaviv & Regev (1994) as well as Brandenburg & Multamäki (2004) for similar results in a different context. However, the assumption of perfect pressure equilibrium is problematic, because then the density is assumed to be inversely proportional to the temperature, so mass conservation is generally not obeyed. In our cases there is no perfect pressure equilibrium and one may argue that the coalescence is primarily the result of individual dense spots moving with the flow toward local and global pressure minima.

It is in principle possible that the amount of viscous heating might suffice to heat the cold patches enough to make them unstable again. However, the amount of viscous heating is insufficient in all the cases that we have investigated. Only when an external forcing function is added to give the flow a rms velocity of 10–30 km/s does the total amount of heating become comparable to Γ , that is, the level of the imposed uniform heating. Obviously, we cannot exclude the possibility of TI-driven turbulence for smaller viscosity, smaller thermal diffusivity, or both. It may therefore be useful to revisit this issue in future when simulations at higher resolution become more affordable.

Detailed models of the heating and cooling properties of the warm and cold components of the ISM have been used to calculate the equilibrium curves, which in practice predict the range of stable versus unstable densities, temperatures and pressures in the ISM (see, e.g., Wolfire et al. 1995, 2003). Calculations, such as those presented in this paper, of the onset and nonlinear stages of the TI, are needed in order to investigate the actual equilibrium pressure realized in a system described by a certain equilibrium curve; from this, the characteristic densities, temperatures and filling factors for the warm and cold phases can also be determined.

Our one-dimensional calculations (Figure 5) of the standard model of Wolfire et al. (1995) show that the mean pressure realized in the unstable regime remains roughly constant at 1750 K cm^{-3} over the whole range of unstable densities, $\langle \rho \rangle = (1-5) \times 10^{-24} \text{ g cm}^{-3}$, and that the pressure is close to the minimal value of 1540 K cm^{-3} . We note, however, that the equilibrium curve differs from the original one because we have used $\mu=0.62$ instead of $\mu=1$, and it also differs somewhat from Sánchez-Salcedo et al. (2002) as we have used revised coefficients based on more accurate continuity considerations. The corresponding temperatures and number densities at this equilibrium pressure are $T_C = 126 \text{ K}$, $n_C = 8.6 \text{ cm}^{-3}$ and $T_W = 9430 \text{ K}$, $n_W = 0.1 \text{ cm}^{-3}$. This behavior carries over into the three-dimensional regime. The calculations with forced turbulence, where the strongest forcing results in turbulent pressures exceeding the thermal pressure by a factor of $\lesssim 3$ show that the mean pressure increases only by about 25%, even though the level of turbulence is relatively strong. The mean pressure obtained in this case in the three-dimensional calculations is roughly 2170 K cm^{-3} , which is in agreement with the observed median pressure of $p/k_B \approx 2250 \text{ K cm}^{-3}$ from Jenkins & Tripp (2001).

We thank the referee for detailed comments, which have motivated us to consider higher resolution runs and helped us to improve the paper. MJK and AJM thank Nordita for hospitality during the course of this study. This work was supported by the Academy of Finland through grant 1112020 (MJK) and the Particle Physics and Astronomy Research Council through grant PPA/S/S/2002/03473 (AJM). The Danish Center for Scientific Computing is acknowledged for granting time on the Horseshoe and Steno clusters.

REFERENCES

- Audit, E., & Hennebelle, P. 2005, *A&A*, 433, 1
 Brandenburg, A., & Dobler, W. 2002, *Comp. Phys. Comm.*, 147, 471
 Brandenburg, A., & Multamäki, T. 2004, *Int. J. Astrobiol.*, 3, 209
 Brandenburg, A., Nordlund, Å., Stein, R. F., & Torkelsson, U. 1995, *ApJ*, 446, 741
 Cox, D. P. 2005, *ARA&A*, 43, 337
 Elphick, C., Regev, O., & Spiegel, E. A. 1991, *MNRAS*, 250, 617
 Elphick, C., Regev, O., & Shaviv, N. 1992, *ApJ*, 392, 106
 Field, G. B. 1965, *ApJ*, 142, 531
 Field, G. B., Goldsmith, D. W., & Habing, H. J. 1969, *ApJ*, 155, L149 (FGH)
 Gazol, A., Vázquez-Semadeni, E., Kim, J. 2005, *ApJ*, 630, 911
 Gammie, C. F. 2001, *ApJ*, 553, 174
 Haugen, N. E. L., & Brandenburg, A. 2004, *PRE*, 70, 026405
 Hawley, J. F., Gammie, C. F., & Balbus, S. A. 1995, *ApJ*, 440, 742
 Jenkins, E. B., & Tripp, T. M. 2001, *ApJS*, 137, 297
 Kerr, R. M. 1996, *JFM*, 310, 139
 Korpi, M. J., Brandenburg, A., Shukurov, A., Tuominen, I., & Nordlund, Å. 1999, *ApJ*, 514, L99
 Koyama, H., & Inutsuka, S.-I. 2002, *ApJ*, 564, L97
 Koyama, H., & Inutsuka, S.-I. 2004, *ApJ*, 602, L25
 Koyama, H., & Inutsuka, S.-I. 2006, *ApJ* (astro-ph/0605528)
 Kritsuk, A. G., & Norman, M. L. 2002a, *ApJ*, 569, L127
 Kritsuk, A. G., & Norman, M. L. 2002b, *ApJ*, 580, L51
 Kritsuk, A. G., & Norman, M. L. 2004, *ApJ*, 601, L55
 Mac Low, M.-M., Klessen, R. S., & Burkert, A. 1998, *PRL*, 80, 2754
 Mac Low, M.-M., Balsara, D. S., Kim, J., & de Avillez, M. A. 2005, *ApJ*, 626, 864
 McKee, C. F., & Ostriker, J. P. 1977, *ApJ*, 218, 148
 Murray, S. D., White, S. D. M., Blondin, J. M., & Lin, D. N. C. 1993, *ApJ*, 407, 588
 Piontek, R. A., & Ostriker, E. C. 2004, *ApJ*, 601, 905
 Piontek, R. A., & Ostriker, E. C. 2005, *ApJ*, 629, 849
 Sánchez-Salcedo, F. J., Vázquez-Semadeni, E., & Gazol, A. 2002, *ApJ*, 577, 768
 Shaviv, N. J., & Regev, O. 1994, *PRE*, 50, 2048
 Vázquez-Semadeni E., Gazol, A., & Scalo, J. 2000, *ApJ*, 540, 271
 Wada, K., Spaans, M., & Kim, S. 2000, *ApJ*, 540, 797
 Wolfire, M. G., Hollenbach, D., McKee, C. F., Tielens, A. G. G. M., & Bakes, E. L. O. 1995, *ApJ*, 443, 152
 Wolfire, M. G., McKee, C. F., Hollenbach, D., & Tielens, A. G. G. M. 2003, *ApJ*, 587, 278